A Four-Grating Interferometer for X-ray Multi-Contrast Imaging

Houxun Miao[a)]

General Optics, LLC., 11955 Eaglerun Way, Zionsville, IN 46077, USA

James C. Williams, Jr.

Department of Anatomy, Cell Biology & Physiology, Indiana University School of Medicine, Indianapolis, IN, 46202 USA

Daniel Josell

Materials Science and Engineering Division, National Institute of Standards and Technology, Gaithersburg, MD 20899, USA

[a)]Author to whom correspondence should be addressed. Email address: houxun.miao@geneoptics.com

ABSTRACT

Background: X-ray multi-contrast imaging with gratings provides a practical method to detect differential phase and dark-field contrast images in addition to the X-ray absorption image traditionally obtained in laboratory or hospital environment. Systems have been developed for preclinical applications in areas including breast imaging, lung imaging, rheumatoid arthritis hand imaging and kidney stone imaging.

Purpose: Prevailing X-ray interferometers for multi-contrast imaging include Talbot-Lau interferometers and universal moiré effect-based phase-grating interferometers. Talbot-Lau interferometers suffer from conflict between high interferometer sensitivity and large field of view (FOV) of the object being imaged. A small period analyzer grating is necessary to simultaneously achieve high sensitivity and large FOV within a compact imaging system but is technically challenging to produce for high X-ray energies. Phase-grating interferometers suffer from an intrinsic fringe period ranging from a few micrometers to several hundred micrometers that can hardly be resolved by large area flat panel X-ray detectors. The purpose of this work is to introduce a four-grating X-ray interferometer that simultaneously allows high sensitivity and large FOV, without the need for a small period analyzer grating.

Methods: The four-grating interferometer consists of a source grating placed downstream of and close to the X-ray source, a pair of phase gratings separated by a fixed distance placed downstream of the source grating, and an analyzer grating placed upstream of and close to the X-ray detector. The object to be imaged is placed upstream of and close to the phase-grating pair. The distance between the source grating and the phase-grating pair is designed to be far larger than that between the phase-grating pair and the analyzer grating to promote simultaneously high sensitivity and large FOV. The method was evaluated by constructing a four-grating interferometer with an 8 μm period source grating, a pair of phase gratings of 2.4 μm period, and an 8 μm period analyzer grating.

Results: The fringe visibility of the four-grating interferometer was measured to be ≈ 24 % at 40 kV and ≈ 18 % at 50 kV X-ray tube operating voltage. A quartz bead of 6 mm diameter was imaged to compare the

theoretical and experimental phase contrast signal with good agreement. Kidney stone specimens were imaged to demonstrate the potential of such a system for classification of kidney stones.

Conclusions: The proposed four-grating interferometer geometry enables a compact X-ray multi-contrast imaging system with simultaneously high sensitivity and large FOV. Relaxation of the requirement for a small period analyzer grating makes it particularly suitable for high X-ray energy applications such as abdomen and chest imaging.

Key words: X-ray multi-contrast imaging, X-ray interferometer, X-ray gratings

1. INTRODUCTION

X-ray multi-contrast imaging, detecting the phase difference introduced by different materials and the scattering introduced by abrupt phase change in addition to the absorption, has the potential to substantially improve the performance and scope of diagnostic radiology. In recent years, research has translated X-ray multi-contrast imaging from laboratory to preclinical/clinical applications. X-Ray interferometers have been installed into commercial digital mammography or tomosynthesis scanners to improve the detection of breast cancers [1, 2]. A prototype dark-field lung imaging system has been developed to improve the early detection of chronic obstructive pulmonary disease (COPD) [3]. An X-ray phase contrast hand imaging system has been developed to evaluate the cartilage in rheumatoid arthritis patients [4]. Prototype imaging systems have been constructed to classify kidney stones [5, 6]. Sophisticated phase stepping techniques, such as electro-magnetic phase stepping [7] and fast acquisition with seamless stage translation (FASST) [8], have been developed to reduce the acquisition time of a multi-contrast imaging system to a few seconds, making X-ray multi-contrast imaging a practical imaging modality for various clinical scans.

Among various X-ray multi-contrast imaging techniques [9-17], universal moiré effect-based phase-grating interferometers [16, 17] and Talbot-Lau interferometers [15] facilitate the use of compact laboratory or medical X-ray tubes and make X-ray multi-contrast imaging practical in a laboratory or hospital environment. The polychromatic far-field interferometer (PFI) [16] with three phase gratings provides the highest sensitivity (typically at least one order of magnitude higher than that of a Talbot-Lau interferometer) among all reported grating-based interferometers. However, the intrinsic fringe period of such an interferometer is typically several hundred micrometers (e.g. ≈ 300 μm in [16] with ≈ 2 m source-to-detector distance) and thus not well resolvable by high energy, large area flat panel X-ray detectors with a typical pixel size of ≈ 100 μm or larger, unless very long source-to-detector distance is used. The dual-phase-grating X-ray interferometer [17-20] has the simplest system geometry and introduces the least loss and spectral response degradation to the imaging system. However, it requires high coherence of the x-ray source with a focal spot size preferably less than half of the source period [17], and the interferometer

sensitivity, which is inversely proportional to the source period, is typically very low. A Talbot-Lau interferometer utilizes the Talbot self-imaging effect of the phase grating at certain fractional Talbot distances to generate the fringe at the detector. The requirements of spatially coherent X-ray source and small fringe period at the detector are eliminated through use of a source grating and an analyzer grating [15]. The major limit of a Talbot-Lau interferometer is the conflict between high interferometer sensitivity and large field of view (FOV). The maximum interferometer sensitivity of a Talbot-Lau interferometer is proportional to the phase grating-to-analyzer grating distance and inversely proportional to the period of the analyzer grating. For imaging, if the object is placed upstream of the phase grating, the sensitivity of the interferometer at the object is scaled down by the ratio of the source grating-to-object and source grating-to-phase grating distances. If the object is placed downstream from the phase grating, the sensitivity is scaled down by the ratio of the object-to-analyzer grating and phase grating-to-analyzer grating distances. In both cases, maximum sensitivity is achieved when the object is placed immediately adjacent to the phase grating. As long as all gratings are larger than the X-ray detector, the FOV is the detector area scaled down by the square of the ratio of the X-ray source-to-object and source-to-detector distances; for FOV sufficient for abdominal and chest X-rays a patient must be positioned close to the detector (i.e., far from the source). If the patient is downstream of the phase grating it is evident that any location sacrifices either FOV or interferometer sensitivity. If the patient is upstream of the phase grating the distance between the phase and analyzer gratings must be minimized for large FOV. However, decreasing the distance between these gratings reduces the maximum sensitivity of the interferometer. The sensitivity at the patient is reduced due to the enlarged source grating period needed to satisfy the Talbot-Lau condition, although the distance from the source grating to the patient is increased. In either case, simultaneous optimization of both sensitivity and FOV is impossible.

Because of practical patient-to-detector and source-to-detector distance restrictions, high interferometer sensitivity requires analyzer gratings with micrometer-scale periods. Coupling the small period with the need for a sufficiently thick layer of high atomic number material to absorb the X-ray photons (e.g., 50 μm

Au for 30 keV X-rays and 200 μm Au for 60 keV X-rays), high aspect ratio X-ray gratings are necessary in a Talbot-Lau interferometer to realize a compact, highly sensitive X-ray multi-contrast imaging system. Fabrication of small period and high aspect ratio analyzer gratings [21-31] is a major challenge in the development of Talbot-Lau interferometers for high energy clinical applications such as abdominal and pulmonary imaging.

The purpose of this article is to report a four-grating interferometer for X-ray multi-contrast imaging that simultaneously provides high interferometer sensitivity and large FOV with X-ray absorption gratings whose features (i.e., trenches) are of moderate aspect ratio. The interferometer consists of a source absorption grating, a pair of phase gratings and an analyzer absorption grating. The phase moiré pattern [17] of the phase grating pair is resolved by the analyzer grating and X-ray detector via heterodyne detection. The source grating ensures the interferogram from each virtual line source constructs in phase. The phase grating pair is placed upstream of and very close to the analyzer grating to increase both the interferometer sensitivity and the FOV.

2. METHODS

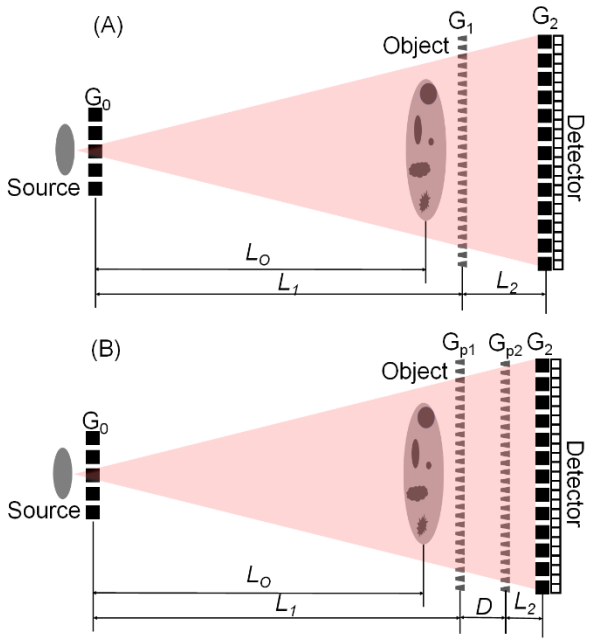

Figure 1. (A) Scheme of a Talbot-Lau interferometer. (B) Scheme of the four-grating interferometer. In both geometries, arrays of gold-filled trenches are patterned at a period of p_0 on the source absorption grating and p_2 on the analyzer absorption grating at the detector. The use of absorption gratings having equal period necessarily requires $L_1 = L_2$, decreasing field of view, in the three-grating geometry given the Talbot-Lau geometric constraint. The use of two phase shift gratings with different periods p_{p1} and p_{p2} in the four-grating system allows larger p_2 of the analyzer grating without loss of sensitivity, simplifying fabrication. Furthermore, whether p_{p1} equals p_{p2} or not, Eqs. 1 and 2 impose no restriction on L_1 and L_2; as such $L_1 >> L_2$ is permitted (i.e., the object can also be very close to the analyzer grating and detector) as required for large FOV and utilized in the experiments detailed in this work.

Figure 1 shows the schemes of a Talbot-Lau interferometer (A) and the proposed four-grating interferometer (B). The geometric sensitivities of both interferometers are determined by the x-ray beam splitting introduced by the grating(s) at the imaging object. The physics can be most readily understood if the imaged object is placed downstream of the phase grating(s). The phase grating pitch and system dimensions are selected (vide infra) such that at any point on the analyzer grating the pair of interfering beams from the

phase grating(s) are angularly separated by λ/p_2, thus creating an interferogram of period p_2 at the analyzer grating plane, where λ is the x-ray wavelength and p_2 is the period of the analyzer grating. Appropriate for the small angles, the beam separation at the imaged object is equal to this angular separation multiplied by the distance between the object and the analyzer grating. The differential phase signal measures the phase difference of these laterally separated interfering beams after they have passed through the object. Under the linear phase approximation within the microscale beam splitting distance, the phase sensitivity is proportional to the beam separation at the imaged object. With these dependencies in mind, by the principle of reciprocity of light propagation, if the object is instead placed upstream of the phase grating(s), the beam separation is proportional to the distance between the object and the source grating and inversely proportional to the source grating period p_0.

For comparison with the optimal configuration in the four-grating system, the imaged object is placed upstream of the phase grating(s) in both systems as illustrated in Fig. 1. The geometric sensitivity of both interferometers is written as L_O/p_0, where L_O is the source grating (G_0)-to-object distance and p_0 is the period of the source grating. The geometric sensitivity represents amplification of the sample-introduced X-ray refraction angle manifest in the measured lateral fringe offset of the interferometer [32]. In Talbot-Lau interferometers, the geometric sensitivity is typically written as L_2/p_2, where L_2 is the phase grating (G_1)-to-analyzer grating (G_2) distance and p_2 is the period of the analyzer grating. This represents the maximum geometric sensitivity of a Talbot-Lau interferometer when the object is placed immediately next to the phase grating. The sensitivity at the imaging object is degraded by the factor L_O/L_1, where L_O is the distance between the source grating (G_0)-and-the object and L_1 is the source grating-to-phase grating distance, as illustrated. The geometric sensitivity at the object, thus proportional to $(L_O/L_1)(L_2/p_2)$, equals L_O/p_0 after imposing the Talbot-Lau geometric constraint [15] $p_0/p_2 = L_1/L_2$, where p_0 is the period of the source grating. Per the physics of the interferometer sensitivity described above, for both interferometers geometry allows the minimum detectable refraction angle α_{min} (in radians) to be related to the pitch of the

source grating, maximum distance between the source grating and imaged object (i.e., source grating to phase grating distance) and x-ray shot noise on each pixel of the detector (expressed in count statistics) as

$$\alpha_{min} = \frac{p_0}{2\pi L_1}\Delta\varphi = \frac{p_0}{2\pi L_1}\frac{\sqrt{2x_{det}}}{V\sqrt{N}}, \quad (1)$$

where, $\Delta\varphi$ is the minimum detectable lateral fringe offset, V is the fringe visibility, N is the number of counts on the detector and x_{det} is the number of counts per incoming photon [33]. Taking the minimum detectable refraction angle as the quantitative measure of the sensitivity of the interferometer-based x-ray phase contrast imaging system, the system sensitivity (inversely proportional to the minimum detectable refraction angle) is thus proportional to the geometric sensitivity, the fringe visibility and the portion of x-ray photons reaching the detector.

The fringe visibilities of a Talbot-Lau interferometer and a two-grating phase moiré interferometer have been well studied [17, 33]. Critically, the two phase gratings in the proposed four-grating interferometer have the same function as the single phase grating in a Talbot-Lau interferometer, i.e., to create a modulated intensity pattern on the analyzer grating. Comparison of the theoretical fringe visibility of the interferometers is thus accomplished by evaluation of the fringe visibilities of a single phase grating Talbot interferometer and a two-grating phase moiré interferometer using point source illumination for idealized grating profiles. For a 50% duty cycle and π phase (shift) grating with a rectangular phase profile, the fringe visibility FV of the Talbot interferometer is given by [33]

$$FV = \frac{\pi}{2}\left|sin^2\left(\frac{\pi\lambda}{2\lambda_0}\right)sin\left(\frac{m\pi\lambda}{2\lambda_0}\right)\right|, \quad (2)$$

where λ is the x-ray wavelength λ_o is the central wavelength of the π phase shift grating and m is the Talbot order. The fringe visibility of a two-grating phase moiré interferometer is given by [17]

$$FV = \left|\frac{1}{p_{p1}p_{p2}}\int_0^{p_{p1}} T_{p1}\left(\xi + \frac{\delta_1 p_{p1}}{2}\right)T_{p1}^*\left(\xi - \frac{\delta_1 p_{p1}}{2}\right)e^{i2\pi\xi f_{p1}}d\xi \int_0^{p_{p2}} T_{p2}\left(\xi + \frac{\delta_2 p_{p2}}{2}\right)T_{p2}^*\left(\xi - \frac{\delta_2 p_{p2}}{2}\right)e^{i2\pi\xi f_{p2}}d\xi\right|, \quad (3)$$

where p_{p1} and p_{p2} are the periods, T_{p1} and T_{p2} are the complex transmission functions, and f_{p1} and f_{p2} are the spatial frequencies (i.e., inverse periods) of the two phase gratings. The parameters δ_1 and δ_2 are given by

$$\delta_{1(2)} = \frac{\lambda}{Lcos^3\theta} f_{1(2)} L_{1(2)} \left[\left(f_{1(2)} - f_{2(1)} \right) L_{2(1)} + f_{1(2)} D \right], \quad (4)$$

where the geometric parameter L is the distance between the source grating and the analyzer grating, D and $L_{1(2)}$ are distances illustrated in Fig. 1B, and θ is the angle of inclination of the line connecting the source and the point of interest on the detector from the linear axis of the system [17]. The polychromatic performance is examined using Gaussian spectra with a full-width-half-maximum (FWHM) of ΔE and central energy of E_0 in the numerical calculation. The fringe visibilities of both interferometers under polychromatic source illumination can be calculated using the weighted average of the fringe visibility across the x-ray spectrum. Fig. 2 shows the fringe visibilities of Talbot interferometers at 1st and 3rd orders, and a two grating phase moiré interferometer with optimized δ_1 and δ_2 of 0.345 for specific grating profiles. The phase grating in the Talbot interferometer has a rectangular phase profile with a π phase shift at E_0 and a 50% duty cycle. The dual phase grating interferometer has a richer and more complex design space and usually is not optimized with 50% duty cycle π phase shift gratings. In the calculation in Fig. 2, both phase gratings have rectangular profiles, with a phase shift of 0.65π at E_0 and a duty cycle of 35% (i.e., Si width percentage of an Si/Air grating). As shown, under broadband polychromatic x-ray illumination, the fringe visibility of the two-grating phase moiré interferometer (red curve) lies close to, and generally between, the visibilities predicted for the 1st order Talbot interferometer (black curve) and 3rd order Talbot interferometer (blue curve). Given the similar fringe visibilities, and it being reasonable to assume grating-introduced-photon-loss of the four-grating interferometer differs little from that of a corresponding Talbot-Lau interferometer using the same absorption grating set, it is rational to compare geometric sensitivities alone to compare performance of the two systems.

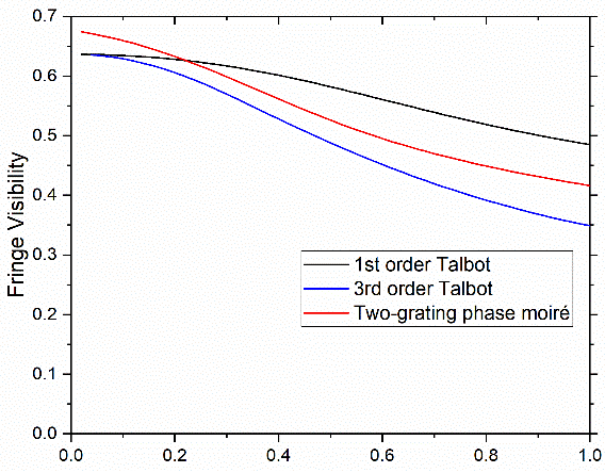

Figure 2. Numerical comparison of fringe visibilities of 1st order Talbot interferometer (black), 3rd order Talbot interferometer (blue) and a two-grating phase moiré interferometer (red) under polychromatic point source illumination as functions of the source spectral bandwidth.

By simple geometrical considerations the FOV of an object imaged in an X-ray imaging system having a fixed detector size is proportional to the source-to-object distance and inversely proportional to the source-to-detector distance. Assuming projections of all gratings at the detector plane are at least as large as an X-ray detector of width W and height of H and both the X-ray source-to-source grating distance and the analyzer grating-to-detector distance are negligible, the dimensions of the FOV of the interferometer system can be expressed as, $W_{FOV} \approx W L_O / L_{SD}$ and $H_{FOV} \approx H L_O / L_{SD}$, where L_{SD} is the source-to-detector distance with $L_{SD} \approx L_1 + L_2$ in a Talbot-Lau interferometer and $L_{SD} \approx L_1 + D + L_2$ in the four-grating interferometer.

In a Talbot-Lau system with fixed analyzer grating period, increase of the geometric interferometer sensitivity, as defined prior to Eq. 1, requires L_2 be increased, which reduces the FOV if the source-to-detector distance L_{SD} (generally a constraint in imaging system design) is fixed. This conflict between interferometer sensitivity and FOV is intrinsic to a Talbot-Lau interferometer, although it is not as severe in some system designs, especially those for which the source-to-detector distance is large [3]. In particular, for low X-ray energy systems, high interferometer sensitivity with large FOV can readily be achieved using

the combination of a small period analyzer grating and a large period source grating [5, 6, 8]. For high X-ray energy systems, however, manufacture of the small period analyzer grating is problematic given the Au thickness required for absorption increases from ≈ 50 μm to ≈ 200 μm when the X-ray tube voltage is increased from 40 kV to 70 kV. The very high aspect ratio that arises from coupling of small period with increased thickness, in conjunction with the large area required, make fabrication of the analyzer gratings for high energy X-ray applications difficult to address with current fabrication techniques.

In the proposed four-grating interferometer system (Fig. 1B) implementing a universal moiré framework [17], the Talbot-Lau geometric constraint of $p_0/p_2 = L_1/L_2$ is removed through use of a pair of phase gratings. The periods of the source grating p_0 and the analyzer grating p_2 are governed by [17]:

$$p_0 = \frac{p_{p1}p_{p2}(L_1+D+L_2)}{(p_{p2}-p_{p1})L_2+p_{p2}D} \tag{5}$$

and

$$p_2 = \frac{p_{p1}p_{p2}(L_1+D+L_2)}{(p_{p1}-p_{p2})L_1+p_{p1}D} \tag{6}$$

where p_{p1} and p_{p2} are the periods of the phase gratings $\mathrm{G_{p1}}$ and $\mathrm{G_{p2}}$, respectively, L_1 is the distance from source grating $\mathrm{G_0}$ to phase grating $\mathrm{G_{p1}}$, L_2 is the distance from the phase grating $\mathrm{G_{p2}}$ to analyzer grating $\mathrm{G_2}$, and D is the distance between the two phase gratings, as illustrated in Fig. 1. From Eqs. (1) and (5), when the two phase gratings have the same period, the source grating and the analyzer grating have the same period. More effectively, the periods of the phase gratings can be differentiated such that the source grating has a smaller period than the analyzer grating. This promotes high interferometer sensitivity L_1/p_0 through the small period of the source grating while simplifying fabrication of the large area, high energy X-ray analyzer grating through decreased feature aspect ratios given its coarser pitch.

A four-grating interferometer was constructed to validate the concept shown schematically in Fig. 1B. The interferometer consists of a tungsten target X-ray tube (SB-80-1k; Source Ray), a pair of homemade 8 μm period, 94 μm deep Si/Au gratings [31] as the source ($\mathrm{G_0}$) and analyzer ($\mathrm{G_2}$) gratings, a PMPGP2.4μm50kV

moiré phase grating pair of 2.4 μm period (General Optics), and a homemade X-ray detector composed of a DRZ-Std scintillator screen (MCI Optonix), a MVL7000 zoom lens (Thorlabs) and a KiraluxTM 2.3 Megapixel Monochrome CMOS Camera (Thorlabs). The inter-grating distances are L_1 = 0.7 m, L_2 = 0.05 m and D = 0.32 m with the source grating 0.05 m downstream of the X-ray focal spot and the analyzer grating 0.02 m upstream of the scintillator screen. The geometric parameters and grating specifications are summarized in Table 1. The imaged objects were placed upstream of and close to (0.05 m upstream of grating G_{p1} in the current experiments) the moiré phase grating pair. The FOV of the imaging system is approximately 2.7 cm × 3.8 cm, limited by the detector size in the short dimension and grating size in the long dimension.

Table 1. Grating and geometric parameters of the four-grating interferometer.

Gratings	Materials	Period	Thickness
Source grating G_0	Si/Au	8 μm	96 μm
Analyzer grating G_2	Si/Au	8 μm	96 μm
Phase grating G_{p1}	Si/W	2.4 μm	25 μm
Phase grating G_{p2}	Si/W	2.4 μm	50 μm
Inter-grating distances	G_0-G_{p1}: L_1= 0.7 m	G_{p1}-G_{p2}: D = 0.32 m	G_{p2}-G_2: L_2= 0.05 m

To construct the interferometer, the four gratings were first placed at their designed geometric positions with the grating surfaces approximately parallel to each other. Next the gratings were rotated about their normal to bring their lines parallel to each other as determined by minimized rotation of the fringe pattern from the orientation of the absorption gratings. The inter-grating distance of the phase gratings was then fine-tuned to optimize the interferometer fringe visibility. Finally, the normal to the grating surfaces were fine tuned to bring them into parallel with the system and each other as assessed by maximization of the interferometer fringe visibility. Despite the additional phase grating, construction of the interferometer was not substantially more difficult or more time consuming than the construction of a Talbot-Lau interferometer. The cost of the additional phase grating was also not significant as compared to the cost of the absorption gratings let alone the system as whole. Indeed, by enabling the use of coarser pitch absorption gratings, the four-grating system has the potential to actually lower the cost of the full grating set, while providing similar

or better interferometer sensitivity. The interferometer constructed for and used in this study exhibited excellent mechanical stability over a 6-month period without use of a floating optical table.

3. RESULTS

Figure 3 shows the interferogram (left) and the fringe visibility map (right) derived from a series of interferograms in a phase stepping process [13] when the X-ray tube is operated at 50 kV. The central third of the fringe visibility map shows higher fringe visibility than the peripheral region due to the vignetting effect, i.e., increasing misalignment of the radially diverging X-rays within the vertically-oriented, high aspect ratio features of the gratings; this can be reduced or eliminated by bending the gratings. Lower X-ray flux at the four corners further decreases the signal to noise in the fringe visibility map.

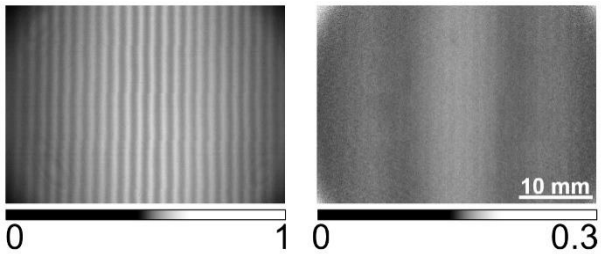

Figure 3. Interferogram (left) and corresponding fringe visibility map (right) of the four-grating interferometer with the X-ray tube operated at 50 kV. The visibility map captures spatial variation of the fringe visibility that reflects the system sensitivity for phase contrast imaging. Increasing misalignment of the high aspect ratio trenches in the gratings and the divergent X-rays reduces the visibility away from the vertical midline of the visibility map, orthogonal to the trenches in the gratings.

Figure 4 shows the average of the fringe visibility across the central third (of the width) of the fringe visibility map at different values of the tube operating voltage. The fringe visibility decreases with the tube voltage because the 94 μm deep Si/Au gratings do not sufficiently absorb the higher energy X-ray photons, and the phase shift provided by the moiré phase grating pair is insufficient for high energy photons. The Si/Au gratings were fabricated via deep reactive ion etching (DRIE) of Si and then filling the trenches with

Au using a robust bottom-up Au filling technique [31]. Use of deeper Si/Au source and analyzer gratings and a moiré phase grating pair for higher energy should provide fringe visibility of > 20 % at 70 kV tube voltage based on much higher fringe visibilities exhibited by 300 μm deep Si/Au gratings fabricated in the same manner [31].

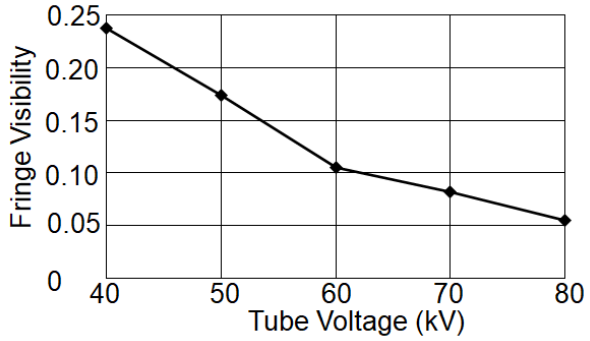

Figure 4. The fringe visibility vs tube voltage curve of the four-grating interferometer. Insufficiently thick Au/Si Absorption gratings and insufficient phase shift through the moiré phase gratings are responsible for the decrease with X-ray tube voltage.

The four-grating X-ray multi-contrast imaging system was first used to image a 6 mm diameter quartz bead at 50 kV tube voltage. Phase stepping was performed to retrieve the multi-contrast images from the raw interferograms; details on the procedure can be found in, e.g., Ref. [13]. The noise floor of the fringe offset is estimated to be 0.065 rad without an imaging object, corresponding to a minimal detectable refraction angle of 118 nrad. Significantly, because only shot noise is considered in Eq. 1, the detector's intrinsic noise may result in underestimation of the intrinsic interferometer sensitivity. Figure 5 shows the processed linear intensity attenuation (i.e., negative log of the measured intensity attenuation), dark-field, differential phase contrast (DPC), and absolute phase shift (via direct integral of the DPC) images. The dark-field signal arises only at the edge of the bead where there is a steep gradient of the refractive index in the direction perpendicular to the lines of the gratings. The stripes in the absolute phase shift image are artifacts resulting from the lack of low-spatial frequency (i.e., wavenumber) information in the DPC signal. The linear attenuation at the sphere centers is 0.80, corresponding to an effective mean X-ray energy of 38.5 keV. The

total phase shift at the sphere centers is estimated to be 405 rad, from which the real part of the refractive index decrement of the quartz material δ is estimated to be 3.5×10^{-7}, close to the tabulated reference value of 3.7×10^{-7} for 38.5 keV photon energy [34].

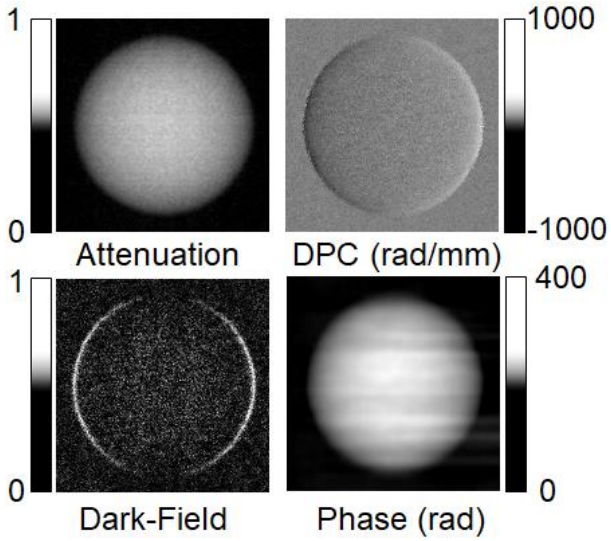

Figure 5. Linear intensity attenuation, differential phase contrast, dark-field and absolute phase shift images of a reference quartz bead of 6 mm diameter.

Consistent with application of the four-grating interferometer for high energy radiography applications such as abdomen imaging and lung imaging [35], the system was used to image several kidney stones (all obtained as de-identified specimens). Figure 6 shows the processed linear intensity attenuation, DPC, absolute phase shift, and dark-field images of a uric acid stone and a calcium oxalate monohydrate (COM) stone. The uric acid stone exhibits a weak linear intensity attenuation signal coupled with a strong dark-field intensity. The COM stone exhibits a strong linear intensity attenuation signal coupled with a weak dark-field signal. The absolute phase shift signals (like the DPC) of the two stones are similar. These three signals are proportional to the path length of X-ray photons when penetrating the specimen. The ratio of the absolute phase shift to the linear intensity attenuation reflects a ratio per thickness that is intrinsic to the specimen material. The ratio of the dark-field intensity to linear attenuation signal is principally determined by the microstructure within the stones (even though that microstructure is not resolved in the X-ray

imaging). Both ratios are independent of the X-ray path length. The dark-field to linear attenuation ratio of the imaged uric acid stone is estimated to be 5.14, while that of the COM is estimated to be 0.57, approximately a factor of 9 lower. The linear attenuation coefficients of uric acid stone ($C_5H_4N_4O_3$, density of 1.85 g/cm^3 used for calculation) and COM ($C_2H_2CaO_5$, density of 2.22 g/cm^3) are 4.56 × 10^{-5} μm^{-1} and 1.65 × 10^{-4} μm^{-1} at 38.5 keV [34], differing by slightly more than a factor of 3. Nonuniformity within the uric acid stone as compared to the more homogeneous microstructures in the COM stone evidently enhances the dark-field signal by an additional factor of 3. The approximately 9× difference of the dark-field to linear attenuation ratios of the uric acid and COM stones, if broadly representative, can be used to distinguish the two types of stones. The absolute phase shift to linear attenuation ratio of the uric acid stone is estimated to be 836 rad, approximately 74 % of the calculated value of 1132 rad [34]. The absolute phase shift to linear attenuation ratio of the COM stone is estimated to be 236 rad, approximately 63 % of the calculated value of 373 rad. The measured absolute phase shift to linear attenuation coefficient of the uric acid stone is approximately 3.54× that of the COM stone (compared to calculated value of 3.03). If more broadly representative this factor could be used in combination with the dark-field to linear attenuation ratio to distinguish more complex stones, such as mixed type stones or stones with similar dark-field to linear attenuation ratio.

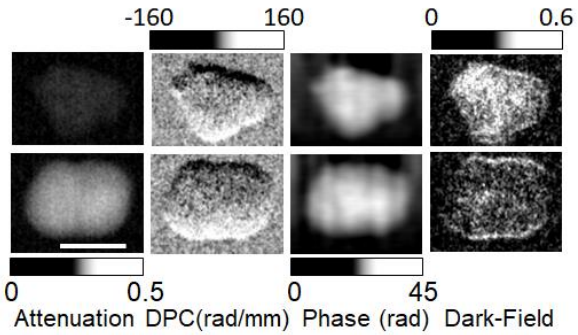

Figure 6. Linear attenuation, differential phase contrast, absolute phase shift and dark-field images of a uric acid stone (top) and a COM stone (bottom). Scale bar under the linear attenuation images is 2 mm.

It was previously stated that the dark-field signal of kidney stones is mainly determined by the internal microstructures of the stones rather than their compositions. Evidence of this is seen in Fig. 7, where dark-field and linear intensity attenuation images of two brushite stones are shown together with their photographic images. The brushite stone in Fig. 7 top panels is more densely packed, as reflected in the strong and more uniform attenuation, and, as such, exhibits a weak dark-field signal. The stone in Fig. 7 bottom panels manifests internal crystal microstructures through the weaker and more variable attenuation, and, as such, exhibits a very strong dark-field signal. The dark-field to linear intensity attenuation ratio is 1.40 and 4.76 for the two stones, respectively. The dark-field to linear intensity attenuation ratio of the crystal brushite stone is comparable to that of the uric acid stone. The two stones can be distinguished by the absolute phase shift to linear attenuation ratio, 836 rad for the uric acid stone and 143 rad for the brushite stone.

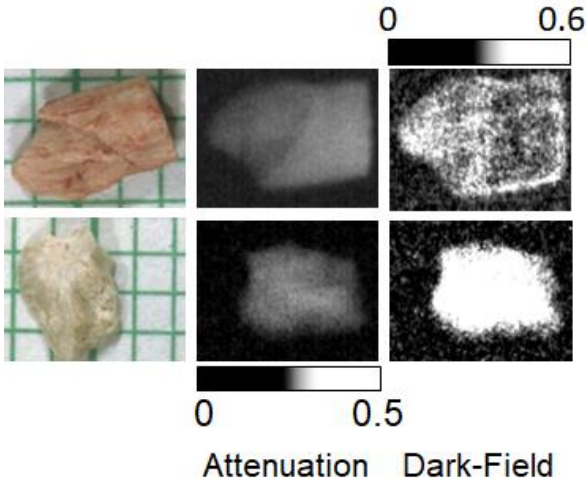

Figure 7. Photos, linear intensity attenuation and dark-field images of a densely packed brushite stone (top) and a brushite stone with significant internal microstructures (bottom). Photos (left) are on paper

4. DISCUSSION

X-ray multi-contrast imaging using a Talbot-Lau three-grating interferometer system in high energy clinical applications is complicated by the restrictions inherent in optimizing the interferometer sensitivity and the

FOV. Increase of both sensitivity and field of view requires the use of smaller period analyzer gratings that are thick enough to fully absorb high energy X-rays, fabrication of which is presently bottlenecked by X-ray absorption grating fabrication techniques. The four-grating interferometer introduced here addresses this conflict by replacing the phase grating with a moiré phase grating pair. The moiré phase grating pair can be placed very close to the detector to simultaneously enlarge the FOV and improve the interferometer sensitivity. In this interferometer configuration, both the interferometer sensitivity and FOV increase monotonically with the distance between the source grating and the object being imaged. In this manner the need for very high aspect ratio analyzer gratings is eliminated.

The four-grating interferometer built for this study utilized a moiré grating pair having a distance D between its gratings that is nearly 30% of the distance between the source and analyzer gratings. This shifts the imaged object closer to the source grating than the analyzer grating, degrading the interferometer sensitivity and reducing the FOV. The FOV achieved here is ≈ 65 % of the detector size in each direction, with the object placed immediately adjacent to the grating $\mathrm{G_{p1}}$, exceeding the ≈ 50 % value of a Talbot-Lau system for the symmetric geometry ($L_1 = L_2$) associated with these absorption gratings ($p_0 = p_2$). The four-grating interferometer effectively shortens the total interferometer distance, while maintaining a high interferometer sensitivity compared to a Talbot-Lau interferometer with the same analyzer grating period and interferometer geometric sensitivity. In the Talbot-Lau interferometer, the distance between the phase grating and the analyzer grating would need to be 0.7 m (assuming fractional Talbot distance condition holds) to meet the same sensitivity requirement. To have a FOV of 65% of the detector size in each direction, the total source grating to analyzer grating distance would have to be 2 m, as compared to the 1.07 m of the four grating interferometer.

The use of moiré phase grating pairs with smaller periods reduces the phase grating spacing D. As one example for pulmonary imaging where the source to detector distance is ideally approximately 2 m, a moiré

grating pair with periods p_{p1} = p_{p2} = 0.9 μm with source and analyzer grating having periods p_0 = p_2 = 30 μm would be associated with a system configuration having L_1 = 1.6 m, D = 0.056 m and L_2 = 0.2 m, allowing placement of the object substantially closer to the analyzer grating. This change would increase the FOV to 86% of the detector size in each direction while simultaneously, a key attribute of the four-grating geometry, increasing the interferometer sensitivity. Such a system will be developed in future work. In an alternative design aiming at higher geometric sensitivity, a moiré grating pair with periods p_{p1} = p_{p2} = 1.6 μm with a source grating and analyzer grating having periods p_0 = p_2 = 16 μm would be associated with a system configuration with L_1 = 1.6 m, D = 0.205 m and L_2 = 0.2 m. This change would increase the geometric sensitivity by 87.5% at the cost of reducing the FOV to 78% of the detector size in each direction. Compared to the Talbot-Lau setup in Ref [36] using a 10 μm period analyzer grating, a 68.72 μm source grating and having a 2 m source-to-detector distance, the geometric sensitivity of the four-grating interferometer is more than 4× that of the Talbot-Lau interferometer for an imaging object placed 1.45 m from the source grating.

More broadly, like a Talbot-Lau interferometer, the four-grating interferometer is well suited for high energy applications, such as abdomen imaging and chest imaging, because the X-ray attenuation introduced by the additional phase grating is negligible at high X-ray energies. The current setup operates at 50 kV X-ray tube voltage, but with Si/Au X-ray gratings of 200 μm to 300 μm depth the operating voltage can be easily extended above 70 kV with a fringe visibility > 20 %, suitable for abdomen imaging and chest imaging.

5. CONCLUSIONS

A four-grating interferometer that enables simultaneous optimization of both sensitivity and field of view without the need for a very small period, high aspect ratio X-ray analyzer grating has been proposed. An interferometer system implementing the four-grating design was constructed to demonstrate highly sensitive X-ray multi-contrast imaging in a compact system. The interferometer has a geometric sensitivity

of up to 8.75×10^4 with an analyzer grating of 8 μm period and 96 μm deep features using a source to detector distance of < 1.2 m. The multi-contrast imaging system described in this work, operating at 50 kV tube voltage, is able to distinguish different types of kidney stones ex-situ. The system can be extended to operate at higher tube voltage for high energy clinical applications using a higher energy X-ray source and thicker analyzer gratings for in-situ examination.

ACKNOWLEGEMENTS

This work was performed in part at the University of Michigan Lurie Nanofabrication Facility. We acknowledge Dr. Jorge Barreda for fabrication assistance. Certain equipment, instruments, software, or materials are identified in this paper in order to specify the experimental procedure adequately. Such identification is not intended to imply recommendation or endorsement of any product or service by NIST, nor is it intended to imply that the materials or equipment identified are necessarily the best available for the purpose.

CONFLICT OF INTEREST

H.M. is the inventor of a patent by General Optics, LLC for the four-grating interferometer.

REFERENCES

1. Li K, Zhang R, Garrett J, Ge Y, Ji X, Chen GH. Design, construction, and initial results of a prototype multi-contrast X-ray breast imaging system. *In Medical Imaging 2018: Physics of Medical Imaging* 2018 Mar 9; Vol. 10573, pp. 234-239. SPIE.
2. Arboleda C, Wang Z, Jefimovs K, et al., Towards clinical grating-interferometry mammography. *European radiology*. 2020; 30:1419-1425.

3. Willer K, Fingerle AA, Noichl W, et al., X-ray dark-field chest imaging for detection and quantification of emphysema in patients with chronic obstructive pulmonary disease: a diagnostic accuracy study. *The Lancet Digital Health*. 2021; 3(11): e733-744.
4. Yoshioka H, Kadono Y, Kim YT, et al., Imaging evaluation of the cartilage in rheumatoid arthritis patients with an X-ray phase imaging apparatus based on Talbot-Lau interferometry. *Scientific reports*. 2020; 10(1): 6561.
5. Scherer K, Braig E, Willer K, et al., Non-invasive differentiation of kidney stone types using X-ray dark-field radiography. *Scientific reports*. 2015; 5(1): 9527.
6. Niemann T, Jerjen I, Hefermehl L, Wang Z, Kubik-Huch RA, Stampanoni M. The classification of renal stones by gratings-based dark-field radiography. *Central European Journal of Urology*. 2021; 74(3):453.
7. Miao H, Chen L, Bennett EE, et al., Motionless phase stepping in X-ray phase contrast imaging with a compact source. *Proceedings of the National Academy of Sciences*. 2013; 110(48): 19268-19272.
8. Zhang R, Fowler AM, Wilke LG, et al., Fast acquisition with seamless stage translation (FASST) for a trimodal x-ray breast imaging system. *Medical physics*. 2020; 47(9): 4356-4362.
9. Bonse U, Hart M. An X-ray interferometer. *Applied Physics Letters*. 1965; 6(8): 155-156.
10. Momose A, Fukuda J. Phase-contrast radiographs of nonstained rat cerebellar specimen. *Medical physics*. 1995; 22(4):375-379.
11. Davis TJ, Gao D, Gureyev TE, Stevenson AW, Wilkins SW. Phase-contrast imaging of weakly absorbing materials using hard X-rays. *Nature*. 1995; 373(6515): 595-598.
12. Chapman D, Thomlinson W, Johnston RE, et al., Diffraction enhanced X-ray imaging. *Physics in Medicine & Biology*. 1997; 42(11): 2015.
13. Momose A, Kawamoto S, Koyama I, Hamaishi Y, Takai K, Suzuki Y. Demonstration of X-ray Talbot interferometry. *Japanese Journal of Applied Physics*. 2003; 42(7B): L866.
14. Weitkamp T, Diaz A, David C, et al., X-ray phase imaging with a grating interferometer. *Optics Express*. 2005; 13(16): 6296-6304.

15. Pfeiffer F, Weitkamp T, Bunk O, David C. Phase retrieval and differential phase-contrast imaging with low-brilliance X-ray sources. *Nature Physics*. 2006; 2(4): 258-261.

16. Miao H, Gomella AA, Harmon KJ, Bennett EE, Chedid N, Znati S, Panna A, Foster BA, Bhandarkar P, Wen H. Enhancing tabletop X-ray phase contrast imaging with nano-fabrication. *Scientific Reports*. 2015; 5(1): 13581.

17. Miao H, Panna A, Gomella AA, Bennett EE, Znati S, Chen L, Wen H. A universal moiré effect and application in X-ray phase-contrast imaging. *Nature Physics*. 2016; 12(9): 830-834.

18. Kagias M, Wang Z, Jefimovs K, Stampanoni M. Dual phase grating interferometer for tunable dark-field sensitivity. *Applied Physics Letters*. 2017; 110(1): 014105.

19. Yan A, Wu X, Liu H. Quantitative theory of X-ray interferometers based on dual phase grating: fringe period and visibility. *Optics Express*. 2018; 26(18): 23142-23155.

20. Ge Y, Chen J, Zhu P, Yang J, Deng S, Shi W, Zhang K, Guo J, Zhang H, Zheng H, Liang D. Dual phase grating based X-ray differential phase contrast imaging with source grating: theory and validation. *Optics Express*. 2020; 28(7): 9786-9801.

21. Noda D, Tanaka M, Shimada K, Hattori T. Fabrication of diffraction grating with high aspect ratio using X-ray lithography technique for X-ray phase imaging. *Japanese Journal of Applied Physics*. 2007; 46(2R): 849.

22. Noda D, Tanaka M, Shimada K, Yashiro W, Momose A, Hattori T. Fabrication of large area diffraction grating using LIGA process. *Microsystem Technologies*. 2008; 14: 1311-1315.

23. Mohr J, Grund T, Kunka D, Kenntner J, Leuthold J, Meiser J, Schulz J, Walter M. High aspect ratio gratings for X-ray phase contrast imaging. *AIP Conference Proceedings* 2012 Jul 31 (Vol. 1466, No. 1, pp. 41-50). American Institute of Physics.

24. David C, Bruder J, Rohbeck T, Grünzweig C, Kottler C, Diaz A, Bunk O, Pfeiffer F. Fabrication of diffraction gratings for hard X-ray phase contrast imaging. *Microelectronic Engineering*. 2007; 84(5-8): 1172-1177.

25. Rutishauser S, Bednarzik M, Zanette I, Weitkamp T, Börner M, Mohr J, David C. Fabrication of two-dimensional hard X-ray diffraction gratings. *Microelectronic Engineering*. 2013; 101: 12-16.

26. Rowen AM, Grubbs RK, Coleman JJ, inventors; National Technology, Engineering Solutions of Sandia LLC, assignee. Electroplated Au for conformal coating of high aspect ratio silicon structures. United States patent US 11,053,601. 2021 Jul 6.

27. Kagias M, Wang Z, Guzenko VA, David C, Stampanoni M, Jefimovs K. Fabrication of Au gratings by seedless electroplating for X-ray grating interferometry. *Materials Science in Semiconductor Processing*. 2019; 92: 73-79.

28. Ambrozik S, Moffat TP, Zhang C, Miao H, Josell D. Bottom-up gold filling of high aspect ratio trenches. *Journal of The Electrochemical Society*. 2019; 166(10): D443.

29. Josell D, Ambrozik S, Williams ME, Hollowell AE, Arrington C, Muramoto S, Moffat TP. Exploring the limits of bottom-up gold filling to fabricate diffraction gratings. *Journal of the Electrochemical Society*. 2019; 166(16): D898.

30. Josell D, Shi Z, Jefimovs K, Romano L, Vila-Comamala J, Moffat TP. Pushing the limits of bottom-up gold filling for X-ray grating interferometry. *Journal of The Electrochemical Society*. 2020; 167(13): 132504.

31. Josell D, Osborn WA, Williams ME, Miao H. Robust bottom-up gold filling of deep trenches and gratings. *Journal of The Electrochemical Society*. 2022; 169(3): 032509.

32. Modregger P, Pinzer BR, Thüring T, Rutishauser S., David C., Stampanoni M. Sensitivity of X-ray grating interferometry. *Optics express*. 2011; *19*(19): 18324-18338.

33. Thuering T, Stampanoni, M. Performance and optimization of X-ray grating interferometry. *Philosophical Transactions of the Royal Society A: Mathematical, Physical and Engineering Sciences*. 2014; *372*(2010): 20130027.

34. http://purple.iptm.ru/xcalc/xcalc_mysql/ref_index.php

35. Williams Jr JC, Lingeman JE, Daudon M, Bazin D. Using micro computed tomographic imaging for analyzing kidney stones. *Comptes Rendus. Chimie*. 2021; 24(S2): 1-12.

36. Sauter AP, Andrejewski J, De Marco F, Willer K, Gromann LB, Noichl W, Kriner F, Fischer F, Braun C, Koehler T, Meurer F. Optimization of tube voltage in X-ray dark-field chest radiography. *Scientific Reports*. 2019; 9(1):8699.